



UNIVERSITY OF SUSSEX

1

DOCTORAL THESIS

2

⁴ Optimisation studies and background
⁵ estimation in searches for the supersymmetric
⁶ partner of the top quark in all-hadronic final
⁷ states with the ATLAS Detector at the LHC

8

9 *A thesis submitted in fulfillment of the requirements*
10 *for the degree of Doctor of Philosophy*

11

in the

12

Experimental Particle Physics Research Group

School of Mathematical and Physical Sciences

Author:

14

Fabrizio MIANO

Supervisor:

14

Dr. Fabrizio SALVATORE

15

14th November 2017

Dedicated to my family.

*Have no fear for atomic energy
'cause none of them can stop the
time*

17

Robert Nesta Marley

18

Acknowledgments

- 19 Thanks to every single thing that went wrong. It made me stronger.

Declaration

21 I, Fabrizio MIANO, hereby declare that this thesis, titled, "Optimisation studies and back-
22 ground estimation in searches for the supersymmetric partner of the top quark in all-
23 hadronic final states with the ATLAS Detector at the LHC" has not been and will not be,
24 submitted in whole or in part to another University for the award of any other degree.

25 *Brighton, June 2018*

University of Sussex
School of Mathematical and Physical Sciences
Experimental Particle Physics Research Group

Doctoral Thesis

31
32 Optimisation studies and background estimation in searches for
33 the supersymmetric partner of the top quark in all-hadronic final
34 states with the ATLAS Detector at the LHC

36 by Fabrizio Miano

Abstract

38 This thesis presents searches for supersymmetry in $\sqrt{s} = 13$ TeV proton-proton collisions
39 at the LHC using data collected by the ATLAS detector in 2015, 2016 and 2017. Events
40 with 4 or more jets and missing transverse energy were selected. Kinematic variables were
41 investigated and optimisations were performed to increase the sensitivity to supersym-
42 metric signals. Standard Model backgrounds were estimated by means of Monte Carlo
43 simulations and data-driven techniques. Before analysing the data in the blinded signal
44 regions the agreement between data and background predictions and the extrapolations
45 from control and validation regions to signal regions were validated. The analysis yiel-
46 ded no significant excess in any of the analyses performed. Therefore limits were set and
47 the results were interpreted as lower bounds on the masses of supersymmetric particles
48 in various scenarios and models.

⁴⁹ Contents

⁵⁰	Introduction	1
⁵¹	1 Theoretical Framework of Supersymmetry searches	2
⁵²	1.1 The Standard Model	2
⁵³	1.1.1 Electroweak Symmetry Breaking and the Higgs mechanism	6
⁵⁴	1.1.2 Flaws of the Standard Model	8
⁵⁵	1.2 Supersymmetry	10
⁵⁶	1.2.1 Why SUSY?	11
⁵⁷	1.2.2 Minimal Supersymmetric Standard Model	12
⁵⁸	1.2.3 Third generation SUSY	15
⁵⁹	2 The ATLAS Experiment at the LHC	18
⁶⁰	2.1 The LHC	18
⁶¹	2.2 The ATLAS Detector	20
⁶²	2.2.1 The Magnet System	22
⁶³	2.2.2 The Inner Detector	23
⁶⁴	2.2.3 The Calorimeters	26
⁶⁵	2.2.4 The Muon Spectrometer	27
⁶⁶	2.3 The ATLAS Trigger System	28
⁶⁷	2.3.1 Level 1 Trigger	30
⁶⁸	2.3.2 High-Level Trigger	30
⁶⁹	3 The <i>b</i>-jet Trigger Signature in ATLAS	31
⁷⁰	3.1 Trigger Efficiency	31
⁷¹	4 Event Simulation and Reconstruction	32
⁷²	4.1 Event Generation	32
⁷³	4.1.1 Parton Distribution Functions (PDFs)	32

74	4.1.2 Matrix Element Calculation	32
75	4.1.3 Parton Showers	32
76	4.1.4 Hadronisation	32
77	4.2 Detector Simulation	32
78	5 Stop searches in final states with jets and missing transverse energy	33
79	6 Results and Statistical Intepretations	34
80	Trigger	35
81	Bibliography	36

⁸² **List of Tables**

⁸³ **List of Figures**

⁸⁴ Introduction

⁸⁵ Last thing to write

⁸⁶ **1** | ⁸⁷ **Theoretical Framework of Super-**
⁸⁷ **symmetry searches**

A theory is something nobody believes, except the person who made it. An experiment is something everybody believes, except the person who made it.

Albert Einstein

⁸⁹ The Standard Model (SM) of particle physics is an effective theory that aims to provide
⁹⁰ a general description of fundamental particles and the phenomena we see in nature, i. e.
⁹¹ the way they interact. Unfortunately, our understanding of nature is still limited due to
⁹² some opened question to which the SM is not able to answer to, yet.

⁹³ In this chapter, an overview of the SM will be presented in Section 1.1 together with
⁹⁴ the limitations of such theory and some of the reasons behind the need of an extension.
⁹⁵ For the last decades theoretical physicsts have been trying to provide extensions to the
⁹⁶ SM, the so-called beyond-the-SM theories. Among these, one of the most popular, Super-
⁹⁷ symmetry which will be discussed in Section 1.2.

⁹⁸ 1.1 The Standard Model

⁹⁹ The 20th century can be considered a quantum revolution. Several experiments led to
¹⁰⁰ discoveries which were found to be, together with the formalised theory, a solid base of
¹⁰¹ the Standard Model of particle physics and our description of nature. Several particles
¹⁰² were predicted first by the SM and then experimentally observed e. g. the W and the Z
¹⁰³ bosons, the τ lepton, [6], and more recently the Higgs boson at the LHC discovered by
¹⁰⁴ ATLAS [7] and CMS [8].

¹⁰⁵ The SM lays on a Quantum Field Theory (QFT) where particles are treated like fields.
¹⁰⁶ It can describe three of the four fundamental forces; weak, electromagnetic, and strong.
¹⁰⁷ As of today, gravity is not considered in the SM. Sections 1.1 and 1.1.2 will be focused
¹⁰⁸ on the description of the fields together with the carriers of the information, and on the
¹⁰⁹ limitations that such theory implies, respectively.

¹¹⁰ The most general classification of the particles within the SM can be made by means of
¹¹¹ spin. Fermions have half-integer spin values - and are usually referred to as matter -, and
¹¹² bosons have integer-spin values. A noteworthy subset of bosons is formed by the Spin-1
¹¹³ bosons (also known as gauge bosons). These can be considered the information carriers
¹¹⁴ or, in fact, the mediators of the forces.

¹¹⁵ Fermions

¹¹⁶ Six quarks and six leptons belong to the fermions family. In particular, fermions can be
¹¹⁷ grouped into three generations. Each generation contains four particles; one up- and one
¹¹⁸ down-type quark, one charged lepton and one neutral lepton. The masses of the charged
¹¹⁹ leptons and quarks increase with the generation. The six quarks of the SM can be grouped
¹²⁰ into three doublets:

$$\begin{pmatrix} u \\ d \end{pmatrix}, \quad \begin{pmatrix} c \\ s \end{pmatrix}, \quad \begin{pmatrix} t \\ b \end{pmatrix}$$

¹²¹ The up-type quarks (up, charm, top) have charge $+\frac{2}{3}e$ and the down-type quarks (down,
¹²² strange, beauty/bottom) have charge $-\frac{1}{3}e$, where e is the electron charge. Quarks also
¹²³ have another quantum number that can be seen as the analogue of the electric charge,
¹²⁴ which is the colour charge. This can exist in three different states; "red", "green" and
¹²⁵ "blue". Moreover, as a consequence of *confinement*, which will be discussed later on in
¹²⁶ this section, quarks cannot exist as free particles. They rather group to form hadronic
¹²⁷ matter, also known as *hadrons*. There are two kinds of hadrons; mesons and baryons.
¹²⁸ Mesons are quark-antiquark systems, e.g. the pion, and baryons are three-quark system,
¹²⁹ e.g. protons and neutrons. Quarks and anti-quarks have a baryon number of $\frac{1}{3}$ and $-\frac{1}{3}$,
¹³⁰ respectively.

¹³¹ There are six leptons and they can be classified in charged leptons (electron e , muon
¹³² μ , tau τ) and neutral leptons (electron neutrino ν_e , muon neutrino ν_μ , tau neutrino ν_τ).

$$\begin{pmatrix} \nu_e \\ e^- \end{pmatrix}, \quad \begin{pmatrix} \nu_\mu \\ \mu^- \end{pmatrix}, \quad \begin{pmatrix} \nu_\tau \\ \tau^- \end{pmatrix}$$

¹³³ Each lepton has a characteristic quantum number, called lepton number (L). Negatively
¹³⁴ (positively) charged leptons have $L = -1$ ($L = 1$) and neutral leptons have $L = 0$. The
¹³⁵ lepton number is conserved in all the interactions.

¹³⁶ Forces of Nature

¹³⁷ Forces in the SM are described by gauge theories, where the interactions is mediated by
¹³⁸ a vector gauge boson.

¹³⁹ The electromagnetic force is described by Quantum ElectroDynamics (QED) and, as
¹⁴⁰ its mediator is the photon (γ) which couples to charged particles, it only affects charged
¹⁴¹ leptons and quarks, not neutrinos. They are instead affected by the weak force which is
¹⁴² mediated by the bosons W^\pm and Z^0 .

¹⁴³ The weak interaction is associated with handedness (the projection of a particle spin
¹⁴⁴ onto its direction of motion). Both leptons and quarks have left- and right-handed com-
¹⁴⁵ ponents. However, only the left-handed (right-handed) component for neutrinos (anti-
¹⁴⁶ neutrinos) has been observed. This means that nature prefers to produce left-handed
¹⁴⁷ neutrinos and right-handed anti-neutrinos, which is the so-called parity violation.

¹⁴⁸ The strong interactions, mediated by the gluon (electrically neutral and massless), is
¹⁴⁹ described by Quantum ChromoDynamics (QCD). Its coupling increases with increasing
¹⁵⁰ distance and is smaller at short range. Moreover, due to gluon self interactions, two
¹⁵¹ different phenomena arise; *confinement*: neither quarks nor gluons are observed as free
¹⁵² particles, but only colourless “singlet” states can be observed as “jets”, namely collim-
¹⁵³ ated cone-shaped sprays of hadrons; *asymptotic freedom*: interactions between quarks and
¹⁵⁴ gluons become weaker as the energy scale increases and the corresponding length scale
¹⁵⁵ decreases.

¹⁵⁶ Table 1.1 summarises the forces described in the SM and their mediators’ main char-
¹⁵⁷ acteristics. Finally, the gravitational force, which is believed to be mediated by the grav-
¹⁵⁸ iton, is not included in Table 1.1 as it is not part of the SM.

¹⁵⁹ Symmetries and Gauge Groups

¹⁶⁰ In 1915, the mathematician Emmy Noether (23 March 1882 – 14 April 1935) proved that
¹⁶¹ every differentiable symmetry of the action - defined as the integral over space of a Lag-

Table 1.1: Forces and mediators described by the SM

Force	Name	Symbol	Mass [GeV]	Charge
Electromagnetic	Photon	γ	0	0
Weak	W	W^\pm	80.398	$\pm e$
	Z	Z^0	91.188	0
Strong	Gluon	g	0	0

162 rangian density function - of a physical system has a corresponding conservation law.
163 More generally, a symmetry is a property of a physical system. Under certain transforma-
164 tions this property is preserved.

165 A gauge theory in QFT, is a theory in which the Lagrangian is invariant under a con-
166 tinuous group of local transformation. Group theory was then adopted to describe the
167 symmetries conserved in the SM. The gauge group of the theory is the *Lie Group*. It con-
168 tains all the transformations between possible gauges. The Lie algebra of group generators
169 is therefore associated with any Lie group and for each group generator there emerges a
170 corresponding field: the gauge field. The quanta of the gauge fields are called *gauge bo-*
171 *sons*.

172 The three SM interactions can therefore be mathematically described by the following:

$$U(1)_Y \otimes SU(2)_L \otimes SU(3)_C \quad (1.1)$$

173 Here, Y is the weak hypercharge, used to estimate the correlation between the electric
174 charge (Q) and the third component of the weak isospin (I_3) via the relation $Q = I_3 + Y/2$,
175 where I_3 can either be $\pm 1/2$ or 0 for left-handed and right-handed particles, respectively;
176 C the colour charge and L the left-handedness.

177 As of today, we can describe three of the four forces of nature with group theory. QED
178 is an Abelian gauge theory with $U(1)$ as symmetry group, with the electromagnetic four-
179 potential as its gauge field and with the photon as its gauge boson [9]. The interactions
180 between charged fermions occurs by the exchange of a massless photon.

181 The weak interaction and the strong interactions are non-Abelian gauge theories with
182 gauge groups $SU(2)$ and $SU(3)$, respectively. As a consequence of being non-Abelian
183 the generators commutators are non-vanishing and therefore the gauge bosons can self-
184 interact. The $SU(2)$ generators of the weak interaction are the massless gauge bosons
185 $W_\mu^{\alpha=1,\dots,3}$ and, as mentioned earlier on in this chapter, they violate the parity by acting
186 only on left-handed particles.

¹⁸⁷ The gauge bosons of $SU(3)_C$ are eight massless gluons, $G_\mu^{\alpha=1,\dots,8}$. The strong interaction
¹⁸⁸ does not distinguish left- and right-handed particles. Finally, the Quarks that interact
¹⁸⁹ through weak interaction are mixtures of SM eigenstates as described by the CKM matrix
¹⁹⁰ [10].

¹⁹¹ 1.1.1 Electroweak Symmetry Breaking and the Higgs mechanism

¹⁹² In 1979 Sheldon Glashow, Abdus Salam, and Steven Weinberg were awarded the Nobel
¹⁹³ Prize in Physics for their contributions to the so-called electroweak unification. In
¹⁹⁴ the mathematical description of the SM in 1.1 the electroweak interaction is described by
¹⁹⁵ $U(1)_Y \otimes SU(2)_L$. The electroweak physical bosons W , Z and γ are related to the four
¹⁹⁶ unphysical gauge bosons $W_\mu^{\alpha=1,\dots,3}$ and B_μ^0 . In particular, to obtain the physical bosons
¹⁹⁷ the gauge bosons have to mix as follows:

$$\begin{pmatrix} A_\mu \\ Z_\mu \end{pmatrix} = \begin{pmatrix} \cos \theta_W & \sin \theta_W \\ -\sin \theta_W & \cos \theta_W \end{pmatrix} \begin{pmatrix} B_\mu \\ W_\mu^3 \end{pmatrix} \quad (1.2)$$

¹⁹⁸ Here, θ_W is the so-called *Weinberg angle* which is the angle by which spontaneous sym-
¹⁹⁹ metry breaking rotates the original W_μ^3 and B_μ , producing the physical Z , and the photon.
²⁰⁰ θ_W can be experimentally determined in terms of the coupling strengths of the $B_\mu(g_1)$ and
²⁰¹ the $W_\mu^\alpha(g_2)$ to the fermions using the relation $\tan \theta_W = g_1/g_2$. The field mixing of gauge
²⁰² bosons that gives birth to the physical ones can be mathematically expressed by the fol-
²⁰³ lowing:

$$A_\mu = W_\mu^3 \sin \theta_W + B_\mu \cos \theta_W \quad (1.3)$$

²⁰⁴

$$Z_\mu = W_\mu^3 \cos \theta_W - B_\mu \sin \theta_W \quad (1.4)$$

²⁰⁵ where A_μ and Z_μ represent the photon and the Z boson, respectively. The charged vector
²⁰⁶ bosons, W_μ^\mp , and its complex conjugate are defined as:

$$W_\mu^\pm = \frac{1}{\sqrt{2}} (W_\mu^1 \mp iW_\mu^2) \quad (1.5)$$

²⁰⁷ Mass terms for both gauge bosons and fermionic fields are not invariant under gauge
²⁰⁸ transformations and are therefore forbidden by the electroweak gauge. Nonetheless, it is
²⁰⁹ proven by experiments that W and Z are massive [9], therefore the SM assumption only
²¹⁰ holds if the electroweak symmetry is broken.

²¹¹ The SM Lagrangian can be written as the sum of the various Lagrangians describing
²¹² the three interactions and the masses of the elementary particles as follows:

$$\mathcal{L}_{\text{SM}} = \mathcal{L}_{\text{EWK}} + \mathcal{L}_{\text{QCD}} + \mathcal{L}_{\text{Mass}} \quad (1.6)$$

²¹³ In order for the SM Lagrangian to remain a renormalisable theory, mass terms ($\mathcal{L}_{\text{Mass}}$)
²¹⁴ cannot be inserted by hand. A mechanism, that can preserve the gauge symmetry in
²¹⁵ the SM and, that can solve the inconsistency arisen from the mass difference between
²¹⁶ the gauge bosons and the physical ones, is needed. A British theoretical physicist, Peter
²¹⁷ Higgs (29 May 1929, Newcastle upon Tyne, UK), came up with a brilliant solution for
²¹⁸ which he was awarded the 2013 Physics Nobel Prize. In the 1960s, Higgs proposed that
²¹⁹ broken symmetry in electroweak theory could explain the origin of masses of elementary
²²⁰ particles, and in particular of W and Z bosons: the Higgs mechanism was given birth.
²²¹ The mechanism introduces a scalar field, known as the Higgs field, thought to couple to
²²² both massive fermions and bosons.

²²³ In the SM the Higgs field is a doublet in $SU(2)$:

$$\phi = \begin{pmatrix} \phi^+ \\ \phi^0 \end{pmatrix} \quad (1.7)$$

²²⁴ with ϕ^+ and ϕ^0 being generic complex fields:

$$\phi^+ = \frac{\phi_1 + i\phi_2}{\sqrt{2}}, \quad \phi^0 = \frac{\phi_3 + i\phi_4}{\sqrt{2}} \quad (1.8)$$

²²⁵ Consider a Lagrangian of the form:

$$\mathcal{L}_{\text{Higgs}} = (\partial_\mu \phi)^* (\partial^\mu \phi) - V(\phi) \quad (1.9)$$

²²⁶ Renormalizability and $SU(2)_L \otimes U(1)_Y$ invariance require the Higgs potential to be of the
²²⁷ following form:

$$V(\phi) = \mu^2 \phi^\dagger \phi + \lambda (\phi^\dagger \phi)^2 \quad (1.10)$$

²²⁸ Eq. 1.9 is the Higgs Lagrangian if ϕ is chosen to be the following:

$$\phi = \begin{pmatrix} \phi^+ \\ \phi^0 \end{pmatrix} = \begin{pmatrix} G^+ \\ \frac{1}{\sqrt{2}}(v + H + iG^0) \end{pmatrix}$$

229 Here, the complex scalar field G^\pm and the real scalar field G^0 correspond to Goldstone
 230 bosons, and the real scalar field H is the SM Higgs boson field [11]. These massless scalars
 231 are absorbed due to the gauge transformations by the electroweak gauge bosons of the SM:

$$\phi = \begin{pmatrix} \phi^+ \\ \phi^0 \end{pmatrix} = \begin{pmatrix} 0 \\ \frac{1}{\sqrt{2}}(v + H) \end{pmatrix} \quad (1.11)$$

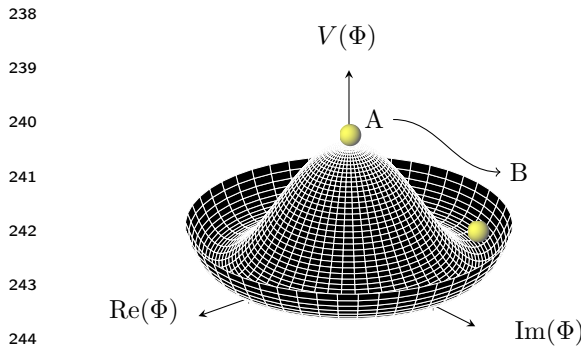
232 The Higgs potential in Eq. 1.10 is displayed in Fig. 1.1 if λ and μ are chosen to be
 233 real. Such potential has a non-zero ground state, v , also known as *vacuum expectation*
 234 *value* (VEV):

$$\phi_0 = \begin{pmatrix} 0 \\ \frac{1}{\sqrt{2}}v \end{pmatrix} \quad (1.12)$$

235 Such representation remains invariant under $U(1)$ allowing electric charge conservation.
 236 However, the SM gauge symmetry 1.1 is broken into $SU(2)_L \otimes U(1)_Y$.

237

In summary, to generate particle masses
 gauge symmetry must be broken. However,
 in order for the theory to remain
 renormalisable, the global Lagrangian
 symmetry must be preserved. This can be
 solved introducing the concept of *spontane-*
ous symmetry breaking (SSB): a mechani-
 sm that allows a symmetric Lagrangian,
 but not a symmetric VEV. In particular,



246 Figure 1.1: The Higgs potential in the complex plane.

247 given a Lagrangian invariant under a cer-
 tain transformation, T_X and a generic set
 248 of states, that transform under T_X as the elements of a multiplet, the symmetry is spon-
 249 taneously broken if one of those states is arbitrarily chosen as the ground state of the sys-
 250 tem. The interaction of the Higgs field with the $SU(2) \otimes U(1)$ gauge fields, $W_\mu^\alpha = 1, 2, 3$,
 251 result in the three gauge bosons fields acquiring mass whilst the B_0 field stays massless.

252 1.1.2 Flaws of the Standard Model

253 During Run 1 and 2 of the LHC, the SM has been extensively validated, as shown in Fig.
 254 1.2: the agreement, between the measured production cross section of various SM pro-
 255 cesses and the SM predictions, looks very good. However, the reasons behind the mass

difference between the three generations of fermions are still not explained by the SM because masses are treated as free parameters of the theory. In addition, there are some fundamental questions that have still no answer and they will be briefly discussed this section.

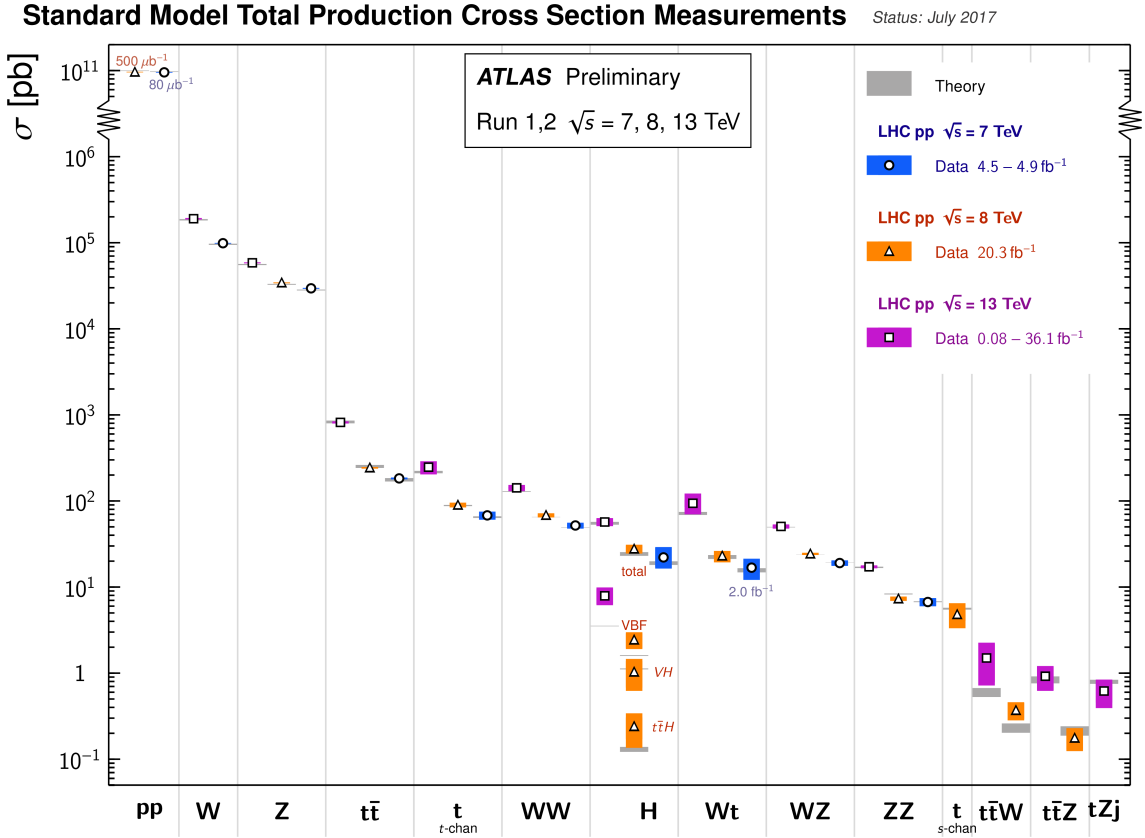


Figure 1.2: Summary of several Standard Model total production cross section measurements, corrected for leptonic branching fractions, compared to the corresponding theoretical expectations. All theoretical expectations were calculated at NLO or higher. The luminosity used for each measurement is indicated close to the data point. Uncertainties for the theoretical predictions are quoted from the original ATLAS papers. They were not always evaluated using the same prescriptions for PDFs and scales. Not all measurements are statistically significant yet [1].

260 Hierarchy Problem

Due to the coupling of the Higgs field to the fermionic fields the one-loop corrections to the Higgs mass receive several contributions. In particular:

$$\Delta m_H^2 = -\frac{|\lambda_f|^2}{8\pi^2} \Lambda_{\text{UV}}^2 + \dots \quad (1.13)$$

here, λ_f is the coupling constant to the fermionic field; Δm_H^2 is the difference between the observed Higgs mass m_H^2 and the bare mass, m_H^0 (Lagrangian parameter); Λ_{UV} is

the ultraviolet momentum cut-off, selected to be at the Planck scale ($\sim 2 \cdot 10^{18}$ GeV), at which a QFT description of gravity is believed to become possible. The correction to the Higgs mass then, will be around 30 orders of magnitude larger than Higgs mass itself, in opposition to what has been measured. This difference just mentioned, between the electroweak scale and the Planck scale arisen from the quantum corrections to the Higgs mass, is the so-called Hierarchy Problem [12].

271 Neutrino Masses

The Super-Kamiokande Collaboration first, in 1998 [13], and SNO Collaboration later, in 2001 [14], have provided measurements of the neutrino flux from solar and atmospheric sources. The Nobel Prize in Physics 2015 was awarded jointly to Takaaki Kajita and Arthur B. McDonald “for the discovery of neutrino oscillations, which shows that neutrinos have mass” [15]. Such feature contradicts the absence of a mechanism for mass generation for the neutrinos.

Various exotic solutions are on the market: one possible solution could be to add the so-called Majorana mass terms for the neutrino (seesaw mechanism). Neutrino physics could unveil physics beyond the SM.

281 Dark Matter

Although dark matter (DM) has never been directly observed, its existence is inferred from its gravitational effects. For example, looking at galaxies rotation, it was observed that the rotation speed was higher than expected, given the amount of visible matter. Two different reasoning arose during the last century to justify such effect either there is matter that cannot be seen by us (in terms of visible light), which contributes to the galactic mass; or the general relativity works differently at galactic distances. The former is believed to be the most likely and it implies the existence of new particles which do not interact via electromagnetic interaction, the so-called Weakly Interacting Massive Particles (WIMPs).

290 1.2 Supersymmetry

Supersymmetry links gravity with the other fundamental forces of nature by introducing a space-time symmetry that relates bosons to fermions and vice-versa, via a transformation of the form of:

$$Q |\text{fermion}\rangle = |\text{boson}\rangle , \quad Q |\text{boson}\rangle = |\text{fermion}\rangle \quad (1.14)$$

294 For each SM particle there exists a superpartner with a spin difference of $\Delta s = 1/2$. As of
 295 today, superpartners, generally called *sparticles* (where the *s* stands for “scalar”), have not
 296 been observed yet, resulting in the assumption that SUSY must be a broken symmetry,
 297 otherwise superpartners would have the same quantum numbers and masses as their
 298 SM equivalent. However, if sparticles were to be too heavy (close to the Planck scale),
 299 the hierarchy problem would still remain unsolved. The *soft* SUSY breaking mechanism
 300 overcomes this problem imposing contrains on the masses of sparticles to a range that can
 301 be experimentally explored.

302 In this section an overview of Supersymmetry (SUSY) will be presented, together with
 303 the motivations behind the success of such theory. Finally, third generation SUSY will be
 304 discussed as it is the most relevant theoretical support to the analyses presented in this
 305 work.

306 1.2.1 Why SUSY?

307 One of the main motivations for SUSY is the cancellation of quadratic divergences to
 308 Δm_H^2 . The introduction of SUSY particles with a half-integer spin difference with re-
 309 spect to their SM provides a solution to the hierarchy problem. The Higgs mass squared
 310 potential receives corrections from a new scalar of mass m_S of the form:

$$\Delta m_H^2 = -\frac{|\lambda_S|^2}{16\pi^2} \left[\Lambda_{UV}^2 - 2m_S^2 \ln(\Lambda_{UV}/m_S) + \dots \right] \quad (1.15)$$

311 where, λ_S is the coupling of SUSY particles to the Higgs field. This term cancels the
 312 fermionic contributions in Eq. 1.13 since the couplings are the same. The experimental
 313 value of Higgs mass will then not need any fine tuning.

314 Fig. 1.3 shows the inverse couplings as a function of the scale for both SM and the
 315 Minimal Supersymmetric Standard Model (MSSM), which will be soon discussed. In the
 316 SM the three lines, representing electromagnetic (dashed blue), weak (dashed red) and
 317 strong (solid green) interactions respectively, do not meet at one point, but with the in-
 318 troduction of supersymmetry, and assuming that the supersymmetric particles are not
 319 heavier than about 1 TeV, they do meet. This is an indication that supersymmetry could
 320 be discovered at the LHC. The possible unification of the coupling constants at the Planck
 321 scale is therefore another good motivation for SUSY searches.

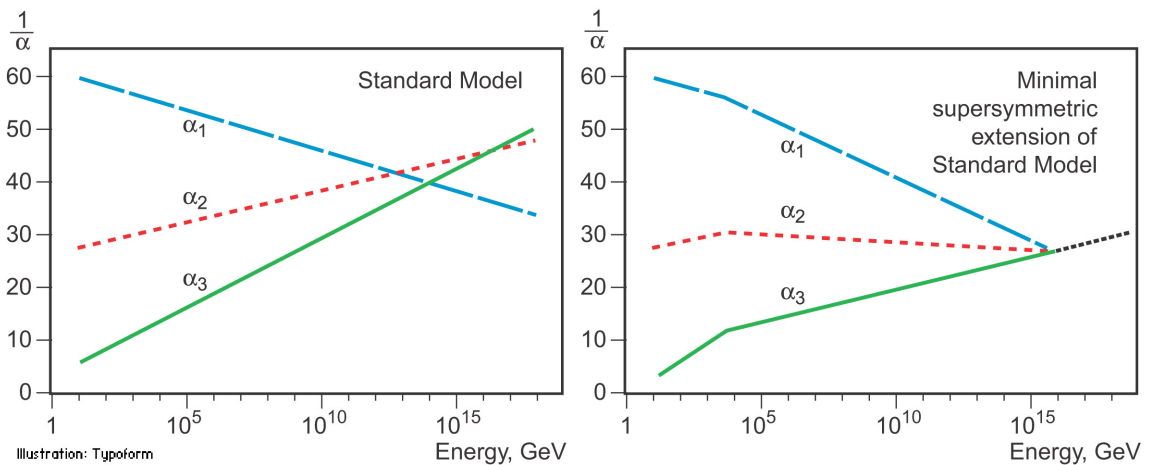


Figure 1.3: The inverse couplings of electromagnetic (dashed blue), weak (dashed red) and strong (solid green) interactions with the SM (left) and a supersymmetric model (right). In the SM the three lines do not meet at one point, but with the introduction of supersymmetry, and assuming that the supersymmetric particles are not heavier than about 1 TeV, they do meet. This is an indication that supersymmetry could be discovered at the LHC.

322 1.2.2 Minimal Supersymmetric Standard Model

323 There does not exist a unique extension of a supersymmetric Standard Model, i.e. SUSY
 324 is not a well-defined model but it is more a framework within which various SM exten-
 325 sions can be derived. The Minimal Supersymmetric Standard Model (MSSM), a minimal
 326 supersymmetric extension of the SM [16], is defined by essentially doubling up the num-
 327 ber of particles in the SM theory in order to include all the SM particles as well as their
 328 corresponding superpartners.

329 Soft SUSY breaking

330 The mass spectrum of the SUSY particles must sit somewhere at a larger scale than the SM
 331 one, as supersymmetric particles have not been discovered at the mass scale of their SM
 332 partners. This gives us a hint that supersymmetry cannot be an exact symmetry, there has
 333 to be an analogous to the electroweak symmetry breaking discussed in 1.1.1 that breaks
 334 SUSY. In particular, this must be soft or spontaneous such that broken supersymmetry still
 335 provides a solution to the hierarchy problem. This means that some new higher energy
 336 scale particles and interactions have to be added to the MSSM, but it also means that
 337 terms, containing only masses and couplings with positive mass dimension, being gauge
 338 invariant and violating SUSY, have to be added to the Lagrangian which will then be

³³⁹ defined as;

$$\mathcal{L} = \mathcal{L}_{\text{SUSY}} + \mathcal{L}_{\text{soft}} \quad (1.16)$$

³⁴⁰ Here, $\mathcal{L}_{\text{SUSY}}$ contains the original SUSY invariant interaction and $\mathcal{L}_{\text{soft}}$ contains all the
³⁴¹ additional terms. A set of around 100 parameters - depending on the method - are then
³⁴² introduced into the theory, and these are catalogued in Table 1.2.

Table 1.2: Main free parameters introduced by soft supersymmetry breaking in the MSSM.

Parameters	Physical Explanation
M_1, M_2, M_3	Bino, Wino and gluino masses
$m_{\tilde{Q}_L}$ $m_{\tilde{u}_R}, m_{\tilde{d}_R}$ $m_{\tilde{l}_L}, m_{\tilde{l}_R}$	left-handed squarks masses up- and down-type right-handed squarks masses left- and right-handed sleptons masses
$m_{\tilde{H}_u^2}, m_{\tilde{H}_d^2}$ $ \mu , B$	Up- and down-type higgsino mass squared higgsino mass and the bilinear higgs term
A_u, A_d, A_e	Up- and down-type squark sfermion and Higgs interaction trilinear couplings
$\tan \beta$	Ratio of the VEVs of the two higgs doublet fields

³⁴³ MSSM mass spectrum

³⁴⁴ As for gauge bosons and the Higgs, there exists MSSM fermionic superpartner. These are
³⁴⁵ referred to as *Gauginos* and *Higgsinos* and, differently from the SM, in the MSSM there are
³⁴⁶ two complex Higgs doublets:

$$H_u = (H_u^+, H_u^0) \quad H_d = (H_d^0, H_d^-)$$

³⁴⁷ with their respective VEVs, v_d, v_u which are constrained by the SM Higgs VEV:

$$v = \sqrt{v_u^2 + v_d^2}$$

³⁴⁸ As per SM gauge bosons, the gaugino masses are affected by electroweak symmetry
³⁴⁹ breaking. The new mass terms, introduced in the $\mathcal{L}_{\text{soft}}$, mix to form the mass eigenstates
³⁵⁰ of the sparticles. Nautral Winos, \tilde{W}^0 , Binos, \tilde{B}^0 and higgsinos \tilde{H}^0 mix to form the four

³⁵¹ neutralinos $\tilde{\chi}_i^0$ ($i = 1, 2, 3, 4$) as it follows;

$$\begin{pmatrix} \tilde{\chi}_1^0 \\ \tilde{\chi}_2^0 \\ \tilde{\chi}_3^0 \\ \tilde{\chi}_4^0 \end{pmatrix} = \begin{pmatrix} M_1 & 0 & -c_\beta s_W m_Z & c_W s_\beta m_Z \\ 0 & M_2 & c_\beta c_W m_Z & -c_W s_\beta m_Z \\ -c_\beta s_W m_Z & c_\beta s_W m_Z & 0 & -\mu \\ s_\beta c_W m_Z & -s_\beta c_W m_Z & -\mu & 0 \end{pmatrix} \begin{pmatrix} \tilde{B}^0 \\ \tilde{W}^0 \\ \tilde{H}_u^0 \\ \tilde{H}_d^0 \end{pmatrix} \quad (1.17)$$

³⁵² Here, $c_\beta = \cos \beta$, $(s_\beta) = \sin \beta$, $c_W = \cos \theta_W$ and $(s_W) = \sin \theta_W$. M_1 , M_2 are related to gaugino masses and μ to higgsino mass, β is the ratio of the electroweak coupling constants and θ_W is the ratio of the VEVs of the two Higgs doublet fields, and finally, m_Z (m_W) is the mass of the Z (W) boson. The neutralino indeces are conventionally assumed to increase with their masses.

³⁵⁷ The charged winos \tilde{W}^\pm and higgsinos \tilde{H}^\pm mix to form four *charginos*, $\tilde{\chi}_i^\pm$ ($i = 1, 2$) as it follows;

$$\begin{pmatrix} \tilde{\chi}_1^\pm \\ \tilde{\chi}_2^\pm \end{pmatrix} = \begin{pmatrix} M_2 & \sqrt{2}m_W \sin \beta \\ \sqrt{2}m_W \cos \beta & \mu \end{pmatrix} \begin{pmatrix} \tilde{W}^\pm \\ \tilde{H}^\pm \end{pmatrix} \quad (1.18)$$

³⁵⁹ Charginos and neutralinos, given birth by the mixing described in Eq. 1.18 and 1.17, will be referred to as bino-like, wino-like or higgsino-like depending on their phenomenology. Gluinos do not mix as they carry colour charge, and its mass is linked to M_3 .

³⁶² Sleptons and squarks states also mix due to electroweak symmetry breaking, although ³⁶³ it is assumed to be zero except for the third generation particles. Stop, \tilde{t}_L , \tilde{t}_R , sbottom \tilde{b}_L , ³⁶⁴ \tilde{b}_R , and stau, $\tilde{\tau}_L$, $\tilde{\tau}_R$ mix to give mass eigenstates, \tilde{t}_1 , \tilde{t}_2 , \tilde{b}_1 , \tilde{b}_2 , $\tilde{\tau}_1$, $\tilde{\tau}_2$, respectively. As with ³⁶⁵ the neutralinos and charginos, the convention is to refer to the one with the lower index as ³⁶⁶ the lighter one. Finally, the Higgs sector is also affected. There are five mass eigenstates, ³⁶⁷ h^0 , H^0 , A^0 , and H^\pm . These, together with the other MSSM particles are listed in Table 1.3.

³⁶⁸ R-parity

³⁶⁹ The most general MSSM can contain operators that violate baryon and / or lepton number, ³⁷⁰ thus allowing proton decays. The non-observation of proton decays forbids the existence ³⁷¹ of such terms. A possibility to avoid these operators is to introduce a new discrete symmetry named R-parity. The conserved quantum number is defined as:

$$P_R = (-1)^{3(B-L)+2s} \quad (1.19)$$

³⁷³ where B , L and s are the baryon, lepton, and spin number, respectively.

Table 1.3: SUSY particles in the MSSM

Name	Spin	Gauge Eigenstates	Mass Eigenstates
Squarks (\tilde{q})	0	$\tilde{u}_L \tilde{u}_R \tilde{d}_L \tilde{d}_R$	(same)
		$\tilde{c}_L \tilde{c}_R \tilde{s}_L \tilde{s}_R$	(same)
		$\tilde{t}_L \tilde{t}_R \tilde{b}_L \tilde{b}_R$	$\tilde{t}_1 \tilde{t}_2 \tilde{b}_1 \tilde{b}_2$
Sleptons (\tilde{l})	0	$\tilde{e}_L \tilde{e}_R \tilde{\nu}_L$	(same)
		$\tilde{\mu}_L \tilde{\mu}_R \tilde{\nu}_L$	(same)
		$\tilde{\tau}_L \tilde{\tau}_R \tilde{\nu}_{\tau}$	$\tilde{\tau}_1 \tilde{\tau}_2 \tilde{\nu}_{\tau}$
Higgs bosons	0	$H_u^0 H_d^0 H_u^+ H_d^-$	$h^0 H^0 A^0 H^{\pm}$
Neutralinos ($\tilde{\chi}_j^0$)	1/2	$\tilde{B}^0 \tilde{W}^0 \tilde{H}_u^0 \tilde{H}_d^0$	$\tilde{\chi}_1^0 \tilde{\chi}_2^0 \tilde{\chi}_3^0 \tilde{\chi}_4^0$
Charginos ($\tilde{\chi}_i^{\pm}$)	1/2	$\tilde{W}^{\pm} \tilde{H}_u^{\pm} \tilde{H}_d^{\mp}$	$\tilde{\chi}_1^{\pm} \tilde{\chi}_2^{\pm}$
Gluino	1/2	\tilde{g}	(same)
Gravitino	3/2	\tilde{G}	(same)

³⁷⁴ If a certain SUSY model is R -parity conserving, then the SM particles have $R = 1$
³⁷⁵ and SUSY partners have $R = -1$. When R -parity conservation is imposed on MSSM
³⁷⁶ models, the mixing between particles and sparticles cannot occur, resulting in the number
³⁷⁷ of SUSY particles to be even at every interaction vertex. Furthermore, all sparticles must
³⁷⁸ be pair-produced and the Lightest Supersymmetric Particle (LSP) has to be stable and
³⁷⁹ can therefore be a good Dark Matter candidate. Heavier sparticles can only decay to odd
³⁸⁰ numbers of it.

³⁸¹ In this work only R -parity conserving (RPC) models, where the $\tilde{\chi}_1^0$ is assumed to be
³⁸² the LSP, were considered.

³⁸³ 1.2.3 Third generation SUSY

³⁸⁴ As mentioned earlier on in this chapter, the introduction of SUSY particles overcomes the
³⁸⁵ problem of an unnatural fine-tuning to the Higgs mass due to its quadratic corrections,
³⁸⁶ given that the stops have masses typically around 1 TeV.

³⁸⁷ Stop pair production analyses are very challenging due to the cross section being
³⁸⁸ around a factor of six smaller than $t\bar{t}$ production (when $m_{\tilde{t}_1} \sim m_t$). Furthermore, the
³⁸⁹ cross-section of such processes dramatically decreases with increasing $m_{\tilde{t}_1}$. Nonethe-
³⁹⁰ less, searches for direct \tilde{t}_1 production with $\tilde{t}_1 \rightarrow t + \tilde{\chi}_1^0$ are sensitive in a scenario where
³⁹¹ $m_{\tilde{t}_1} \gg m_t + m_{\tilde{\chi}_1^0}$ as the large E_T^{miss} , from the neutralinos, provides discriminating power
³⁹² for $t\bar{t}$ rejection.

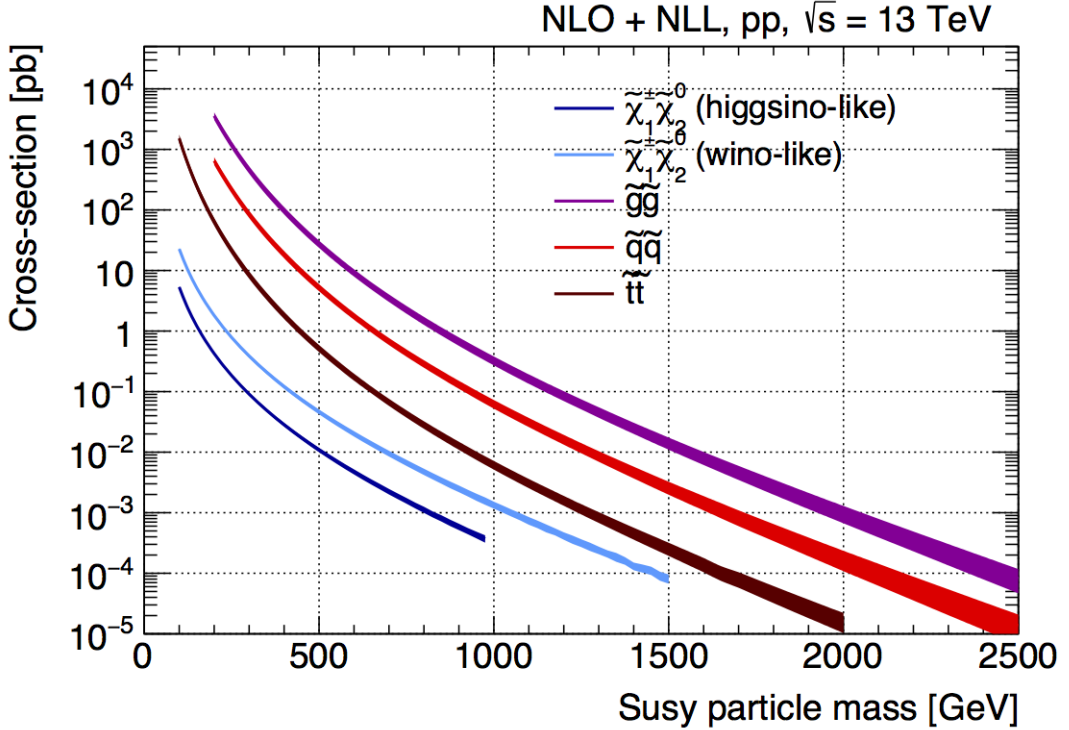


Figure 1.4: NLO+NLL production cross sections as a function of mass at $\sqrt{s} = 13 \text{ TeV}$ [2]

Fig. 1.4 shows SUSY particles production cross-sections for squarks that do not contribute to gluino production diagrams and vice versa, i.e. treating squarks and gluinos as *decoupled* making the cross section of squark pair-production be the same for all families. While gluinos production cross-sections are fairly large, SUSY electroweak production cross-sections of neutralinos and charginos are considerably lower. Sleptons production cross-section, which is not displayed, would sit just below higgsino-like chargino/neutralino production cross-section.

The large number of particles and degrees of freedom in the MSSM brings in some parametrisation issues that lead to a non-trivial theoretical interpretation of the results of a certain analysis. However, simplified models represent a good workaround. The strategy [17] practically is to focus the attention only on a specific signal process without caring about other contributions. The analysis will then be optimised to address that particular signal, e.g. direct stop pair-production in the two-body channel $t \rightarrow \tilde{t}_1 + \tilde{\chi}_1^0$ without including the remaining SUSY mass spectrum. Such simplified models allow a theoretical reinterpretation of the results and provide a powerful tool to constrain various models. In this work only analyses laying their theoretical assumptions on such simplified models will be presented.

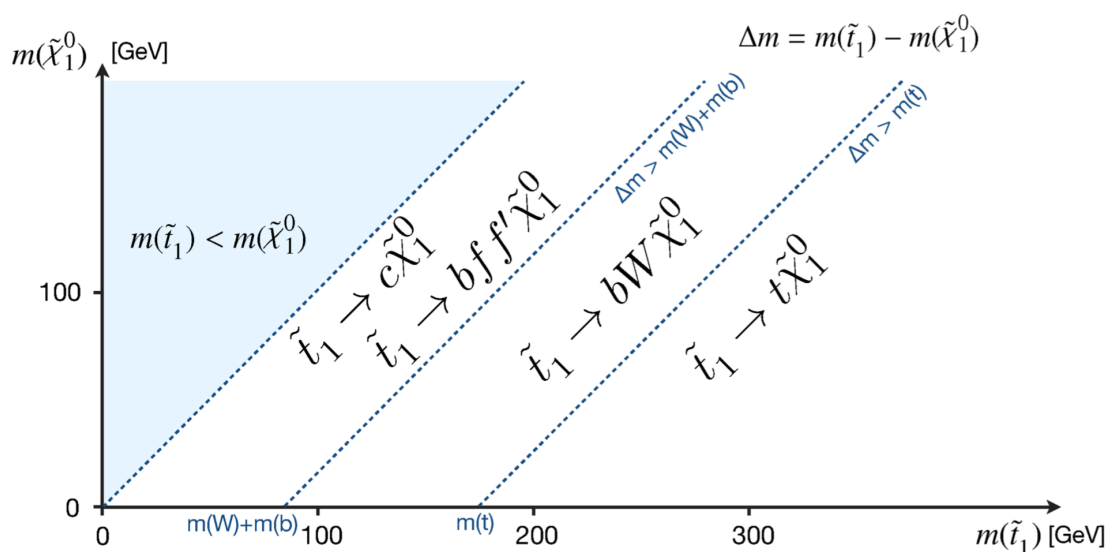


Figure 1.5: Illustration of stop decay modes in the plane stop-neutralino mass plane where the latter is assumed to be the lightest supersymmetric particle and the only one present among the decay products. The dashed blue lines indicate thresholds separating regions where different processes dominate.

⁴¹⁰ **2 | The ATLAS Experiment at the**

⁴¹¹ **LHC**

⁴¹² ATLAS (A Toroidal LHC ApparatuS) is one of the four main experiments (ATLAS, CMS,
⁴¹³ ALICE, LHCb) taking data at a center-of-mass energy of 13 TeV using beams delivered by
⁴¹⁴ the Large Hadron Collider (LHC). In this chapter an overview of the LHC will be given
⁴¹⁵ in Section 2.1, then the ATLAS detector will be described in Section 2.2, and finally the
⁴¹⁶ Trigger system, used to cleverly store the data, will be described in Section 2.3. A more
⁴¹⁷ in-depth description of the Trigger algorithms I have been involved in will be given in
⁴¹⁸ Chapter 3.

⁴¹⁹ **2.1 The LHC**

⁴²⁰ As of today, the LHC is the world's largest and most powerful particle accelerator. It was
⁴²¹ designed to help answer some of the fundamental open questions in particle physics by
⁴²² colliding protons at an unprecedented energy and luminosity. It is located at the European
⁴²³ Organisation for Nuclear Research (CERN), in the Geneva area, at a depth ranging from
⁴²⁴ 50 to 175 metres underground. It consists of a 27-kilometre ring made of superconducting
⁴²⁵ magnets, and inside it two high-energy particle beams travel in opposite directions and
⁴²⁶ in separate beam pipes.

⁴²⁷ The beams are guided around the ring by a strong magnetic field generated by coils -
⁴²⁸ made of special electric cables - that can operate in a superconducting regime. 1232 super-
⁴²⁹ conducting dipole and 392 quadrupole magnets, with an average magnetic field of 8.3 T,
⁴³⁰ are employed and kept at a temperature below 1.7 K, in order to preserve their supercon-
⁴³¹ ducting properties. The formers are used to bend the beams and the latters to keep them
⁴³² focused while they get accelerated.

⁴³³ The collider first went live on September 2008 even though, due to a magnet quench
⁴³⁴ incident that damaged over 50 superconducting magnets, it has been operational since

⁴³⁵ November 2009 when low-energy beams circulated in the tunnel for the first time since the
⁴³⁶ incident. This also marked the start of the main research programme and the beginning
⁴³⁷ of the so-called Run 1: first operational run (2009 - 2013).

⁴³⁸ Performance of the LHC

⁴³⁹ In June 2015 the LHC restarted delivering physics data, after a two-year break, the so-
⁴⁴⁰ called Long Shutdown 1 (LS1), during which the magnets were upgraded to handle the
⁴⁴¹ current required to circulate 7-TeV beams. It was the beginning of the so-called Run 2 -
⁴⁴² second operational run (2015-2018) - during which LHC has collided up to 10^{11} bunches
⁴⁴³ of protons every 25 ns at the design luminosity - the highest luminosity the detector was
⁴⁴⁴ designed to cope with - of $2 \cdot 10^{34} \text{ cm}^{-2} \text{s}^{-1}$. The definition of the luminosity is:

$$\mathcal{L} = f \frac{n_b N_1 N_2}{4\pi \sigma_x \sigma_y} \quad (2.1)$$

⁴⁴⁵ where N_1 and N_2 are the number of protons per bunch in each of the colliding beams, f
⁴⁴⁶ is the revolution frequency of the bunch collisions, n_b the number of proton per bunch,
⁴⁴⁷ and σ_x and σ_y are the horizontal and vertical dimensions of the beam. The luminosity is
⁴⁴⁸ strictly related to the number of collisions occurring during a certain experiment via the
⁴⁴⁹ following:

$$\mathcal{N}_{\text{event}} = \mathcal{L} \sigma_{\text{event}} \quad (2.2)$$

⁴⁵⁰ where σ_{event} is the cross section of the process under investigation. It has not only collided
⁴⁵¹ protons but also heavy ions, in particular lead nuclei at $\sqrt{s_{NN}} = 5.02 \text{ TeV}$, at a luminosity
⁴⁵² of $10^{27} \text{ cm}^{-2} \text{s}^{-1}$ [18].

⁴⁵³ Acceleration stages

⁴⁵⁴ Before reaching the maximum energy, the proton beams are accelerated by smaller ac-
⁴⁵⁵ celerators through various stages. Figure 2.1 shows a sketch of the CERN's accelerator
⁴⁵⁶ complex. It all begins at the linear accelerator LINAC 2. Here protons are accelerated up
⁴⁵⁷ to 50 MeV, and then injected in the Proton Synchrotron Booster (PSB) where they reach
⁴⁵⁸ 1.4 GeV. The next stage is the Proton Synchrotron (PS), which boosts the beams up to 25
⁴⁵⁹ GeV and then the Super Proton Synchrotron (SPS) makes them reach energies up to 450
⁴⁶⁰ GeV. Eventually, the beams are injected in bunches with a 25 ns spacing into the LHC,
⁴⁶¹ where they travel in opposite directions, while they are accelerated to up to 13 TeV. Once

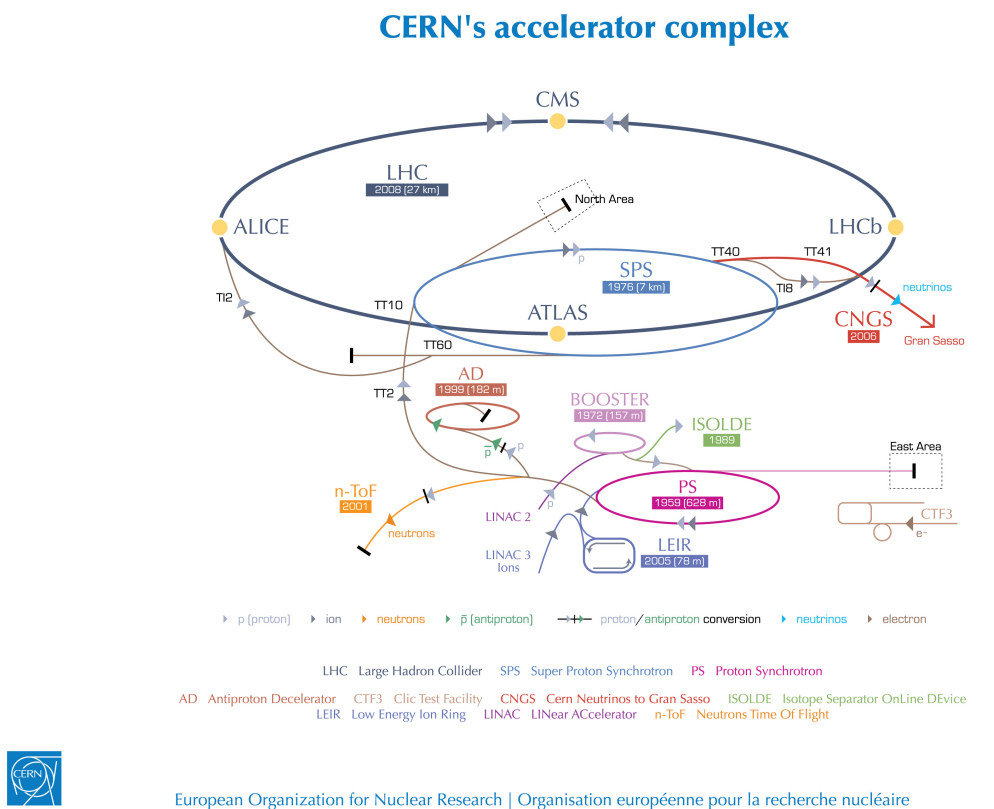


Figure 2.1: CERN Accelerator complex. The LHC is the last ring (dark grey line). Smaller machines are used for early-stage acceleration and also to provide beams for other experiments [3].

462 the bunches reach the maximum energy, they are made collide at four different points,
 463 inside four experiments around the ring [19].

464 The heavy ion beams acceleration procedure is slightly different. Their journey starts
 465 at LINAC 3 first, and the Low Energy Ion Ring (LEIR) then, before they make their way
 466 into the PS where they follow the same path as the protons [19].

467 The four large detectors on the collision points are; the multi-purpose detectors A Tor-
 468 oidal LHC ApparatuS (ATLAS), and Compact Muon Solenoid (CMS) [20], Large Hadron
 469 Collider beauty (LHCb) [21], which focuses on flavour physics, and A Large Ion Collider
 470 Experiment (ALICE) [22] which specialises in heavy ion physics. The *big four* are not the
 471 only experiments at the CERN's accelerator complex. There also are smaller experiments
 472 based at the the four caverns about the collision points e.g. TOTEM, LHCf and MoEDAL,
 473 but this will not be discussed any further in this thesis.

474 2.2 The ATLAS Detector

475 ATLAS is a general-purpose detector designed to collect data with the highest luminosity
 476 provided by the LHC. It is located at CERN's Point 1 cavern and it measures about 45 m in

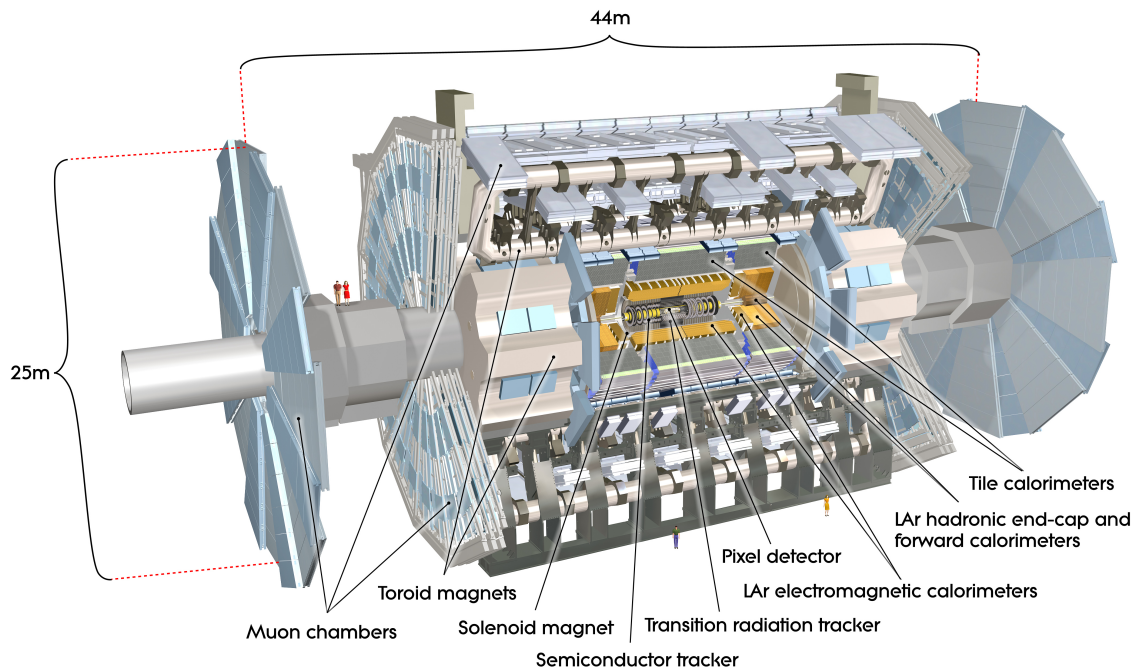


Figure 2.2: Cut-away view of the ATLAS detector. The dimensions of the detector are 25 m in height and 44 m in length. The overall weight of the detector is approximately 7000 tonnes [3].

length and 25 m in diameter. It has a forward-backward symmetric cylindrical geometry with respect to the interaction point and it is designed to reconstruct and measure physics objects such as electrons, muons, photons and hadronic jets. Its design was optimised to be as sensitive as possible to the discovery of the Higgs boson and beyond-the-Standard-Model (BSM) physics. In fact, thanks to the other sub-systems, ATLAS is able to observe all possible decay products by covering nearly 4π steradians of solid angle.

In Figure 2.2 a cut-away view of ATLAS with all its components is shown. The inner-most layer is the Inner Detector (ID) which is the core of the tracking system and consists of a Pixel, a Silicon micro-strip tracker (SCT), and a Transition Radiation Tracker (TRT). It is submerged in a 2 T magnetic field, generated by a thin superconducting solenoid, which bends all the charged particles' trajectories allowing transverse momentum measurement. The electromagnetic and hadronic calorimeters form the next layer and they are both used to perform precise energy measurements of photons, electrons, and hadronic jets. Finally, the outermost layer corresponds to the Muon Spectrometer (MS) which, together with the ID, enclosed in a toroidal magnetic field, allows precise measurement of momentum and position of muons. These sub-detectors will be discussed in more detail in the following sections.

494 The ATLAS coordinate system

495 A coordinate system is taken on for the spatial definition of the sub-systems and kinematic
 496 measurement of physics processes. Such system is defined starting from the interaction
 497 point, defined as the origin. The z -axis is defined by the beam direction and the $x - y$
 498 plan, as transverse to the beam direction.

499 A quantity, known as pseudorapidity, (η), is defined to describe the angle of a particle
 500 coming out of the collision, with respect to the beam axis:

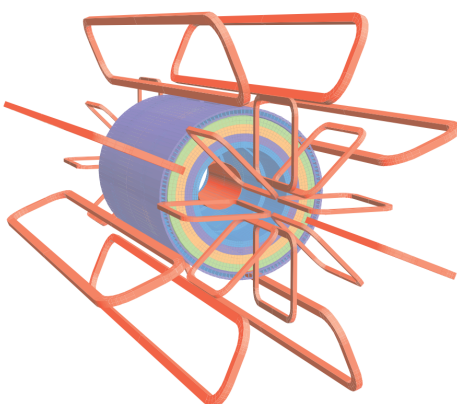
$$\eta \equiv -\ln(\tan(\theta/2))$$

501 Here θ is the polar angle. The azimuthal angle, ϕ , is defined around the beam axis and
 502 the polar angle. In the (η, ϕ) space a distance ΔR can be therefore defined as

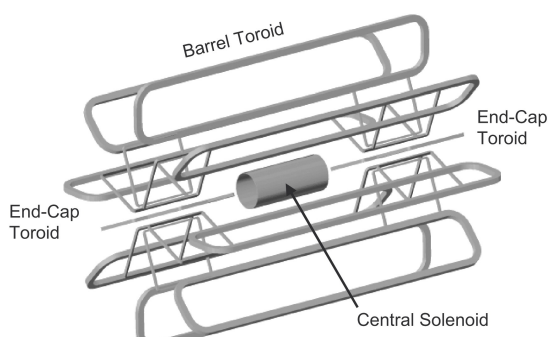
$$\Delta R = \sqrt{\Delta\eta^2 + \Delta\phi^2}$$

503 where $\Delta\eta$ and $\Delta\phi$ are the differences in pseudorapidity and azimuthal angle between any
 504 two considered objects. A central and a forward region of pseudorapidity are also defined
 505 such that the detector components are described as part of the *barrel* if they belong to the
 506 former or as part of the *end-caps* if they belong to the latter.

507 2.2.1 The Magnet System



(a) Geometry of magnet windings and tile calorimeter steel. The eight barrel toroid coils, with the end-cap coils interleaved are visible. The solenoid winding lies inside the calorimeter volume [4].



(b) Schematic view of the superconducting magnets [23].

Figure 2.3: The ATLAS magnet system.

508 The ATLAS magnet system, 26 m long with a 22 m diameter, generates the magnetic field
 509 needed to bend the trajectories of charged particles in order to perform momentum meas-
 510 urement. Figure 2.3a and 2.3b show the geometry of the system and its components,
 511 which are made of NbTi - superconducting material - and will be described in the follow-
 512 ing paragraphs.

513 **The Central Solenoid**

514 With an axial length of 5.8 m, an inner radius of 2.46 m, and an outer radius of 2.56 m, the
 515 central solenoid magnet is located between the ID and the ECAL. Its function is to bend
 516 the charged particles that go through the ID and it is aligned on the beam axis providing
 517 a 2 T axial magnetic field that allows accurate momentum measurement up to 100 GeV
 518 [23].

519 **The Barrel and the End-cap Toroids**

520 Figure 2.3b displays the toroid magnetic system that surrounds the calorimeters. With its
 521 cylindrical shape this component consists of a barrel and two end-caps toroids, each with
 522 eight superconducting coils. The system allows accurate measurement of muon momenta
 523 using a magnetic field of approximately 0.5 T (barrel) for the central regions and 1 T (end-
 524 cap) for the end-cap regions, respectively, which bends the particles in the θ direction.

525 **2.2.2 The Inner Detector**

526 The Inner Detector (ID) [24] is the innermost component of the ATLAS detector i. e. the
 527 nearest sub-detector to the interaction region and it is used to reconstruct charged particle
 528 tracks used in the selection of physics objects. In fact, it allows robust track reconstruction,
 529 with accurate impact parameter resolution ($\sim 20\mu m$) and precise primary and secondary
 530 vertex reconstruction for charged particles (tracks) above 500 MeV and within $|\eta| < 2.5$.

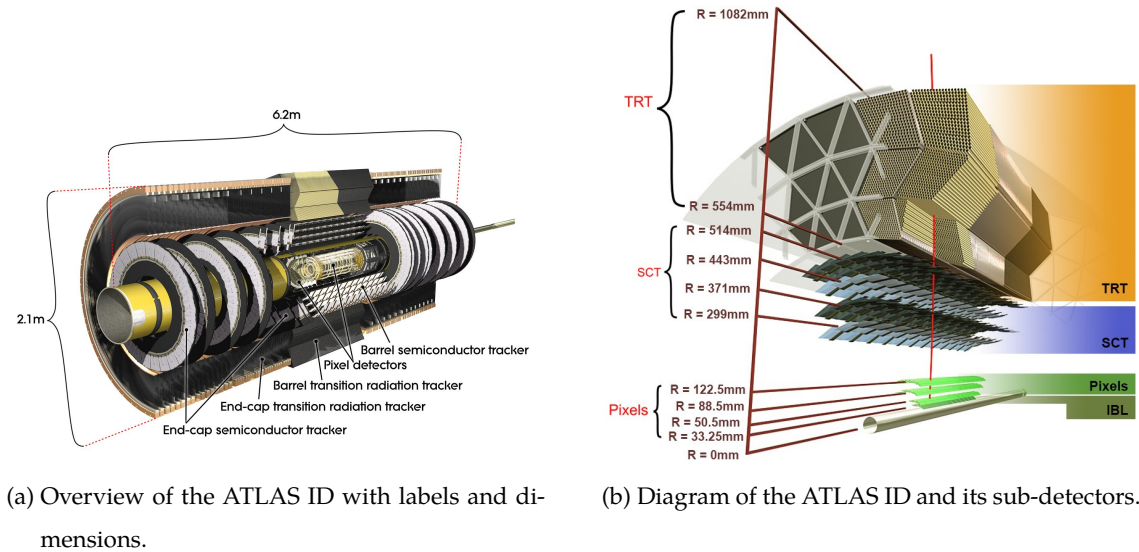
531 The ID is comprised of independent and concentric sub-systems, which are all shown
 532 in Figure 2.4:

- 533 • Insertable B-Layer (IBL):

534 innermost Pixel Detector layer added during ATLAS Run 2 upgrade (2013/2014) to
 535 improve vertexing and impact parameter reconstruction;

- 536 • Silicon Pixel Tracker (Pixel):

537 made of silicon pixel layers and used mainly for reconstructing both the primary



(a) Overview of the ATLAS ID with labels and dimensions.

(b) Diagram of the ATLAS ID and its sub-detectors.

Figure 2.4: The ATLAS Inner Detector

538 and secondary vertices in an event;

539 • SemiConductor Tracker (SCT):

540 comprised of silicon microstrip layers; thanks to its resolution ($17 \times 580 \mu\text{m}$) it can
541 accurately measure particle momenta;

542 • Transition Radiation Tracker (TRT):

543 final layer comprised of various layers of gaseous straw tube elements surrounded
544 by transition radiation material.

545 These sub-detectors will be discussed in the following sections.

546 **IBL**

547 The IBL [25] is the innermost Pixel Detector layer as shown in Figure 2.4b. It is comprised
548 of 6M channels and each pixel measures $50 \times 250 \mu\text{m}$. Its resolution is $8 \times 40 \mu\text{m}$, The
549 addition of this new layer brought a considerable improvement on the performance of the
550 Pixel Detector by enhancing the quality of impact parameter reconstruction of tracks. In
551 particular, this was achieved by improving the vertex finding efficiency and the tagging
552 of bottom-quark-initiated jets (b -jets) which, in case of a B-layer failure, can be restored
553 by the IBL. Besides these improvements, the IBL insertion allowed ATLAS to better cope
554 with high luminosity effects such as the increase in event pile-up, which leads to high
555 occupancy and read-out inefficiency.

556 Pixel

557 The Pixel detector is comprised of 1750 identical sensorchip-hybrid modules, each cover-
 558 ing an active area of 16.4×60.8 mm. The total number of modules correspond to roughly
 559 80 million semiconductor silicon pixels. The nominal pixel size is $50 \mu\text{m}$ in the ϕ direction
 560 and $400 \mu\text{m}$ in the barrel region, along the z -axis (beam axis) [26]. The reason why such a
 561 large amount of pixels is employed is justified by the need to cope with the high luminos-
 562 ity in ATLAS. The silicon pixel detector measures 48.4 cm in diameter and 6.2 m in length
 563 providing a pseudorapidity coverage of $|\eta| < 2.5$. Figure 2.4b shows the three concentric
 564 barrel layers placed at 50.5 mm, 88.5 mm and 122.5 mm respectively. Furthermore, the
 565 Pixel detector is made of six disk layers, three for each forward region, such that when a
 566 charged particle crosses the layers it will generate a signal at least in three space points.
 567 The fine granularity of such detector allows accurate measurement and precise vertex re-
 568 construction, as it provides a more accurate position measurement as a large detection
 569 area is available. In particular, it has a resolution of $10 \times 115 \mu\text{m}$.

570 SCT

571 The SCT is made of 4088 modules of silicon micro-strip detectors arranged in four con-
 572 centric barrel layers. It is mainly used for precise momentum reconstruction over a range
 573 $|\eta| < 2.5$ and it was designed for precision measurement of the position using four points
 574 (corresponding to eight silicon layers), obtained as track hits when crossing the layers.
 575 Figure 2.4b shows the structure of the SCT with its four concentric barrel layers with radii
 576 ranging from 299 mm to 514 mm and two end-cap layers. Each module has an intrinsic
 577 resolution of $17 \mu\text{m}$ in the $R - \phi$ direction and $580 \mu\text{m}$ in the z direction. As the SCT is fur-
 578 ther away from the beam-pipe than the Pixel detector, it has to cope with reduced particle
 579 density. This allows for reduced granularity maintaining the same level of performance of
 580 the Pixel detector: SCT can use ~ 6.3 million read-out channels.

581 TRT

582 The last and outermost of the sub-systems in the ID is the TRT. It is a gaseous detector
 583 which consists of 4 mm diameter straw tubes wound from a multilayer film reinforced
 584 with carbon fibers and containing a $30 \mu\text{m}$ gold plated tungsten wire in the center. The
 585 straw is filled with a gas mixture of 70% Xe, 27% CO₂ and 3% O₂ [27]. As shown in Figure
 586 2.4b, its section consists of three concentric layers with radii ranging from 544 mm to 1082
 587 mm, each of which has 32 modules containing approximately 50,000 straws, 1.44 m in

length, aligned parallel to the beam direction with independent read-out at both ends.
 Both end-cap sections are divided into 14 wheels, with roughly 320,000 straws in the R-direction. The average 36 hits per track in the central region of the TRT allow continuous tracking to enhance pattern recognition and momentum resolution in the $|\eta| < 2.5$ region.
 It also improves the p_T resolution for longer tracks.

2.2.3 The Calorimeters

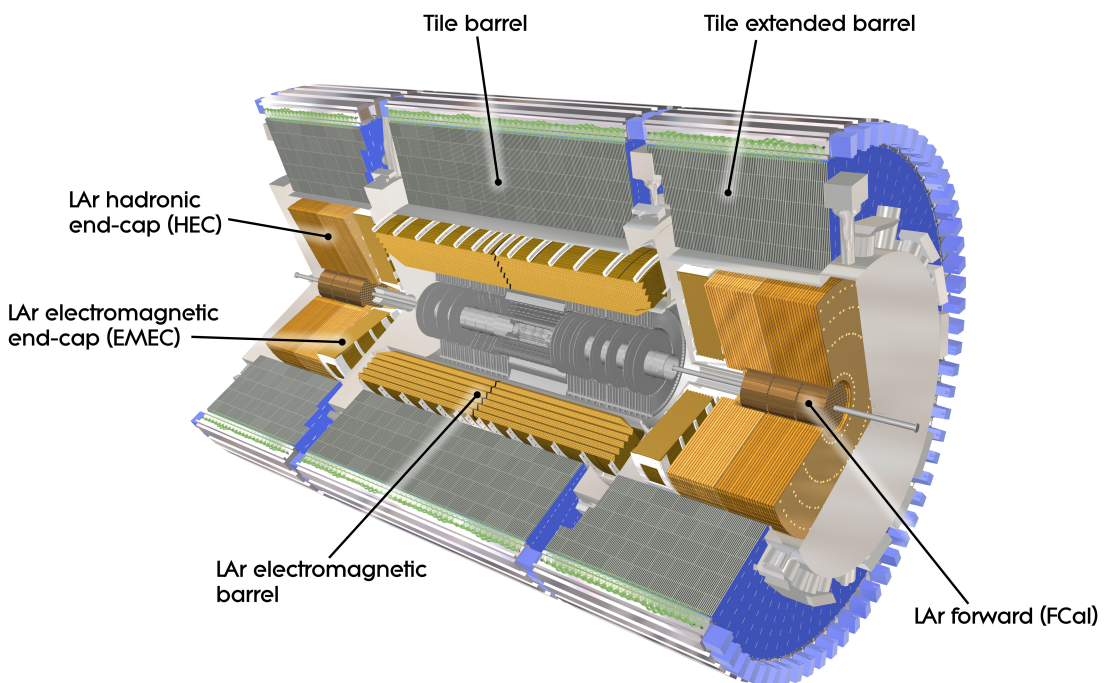


Figure 2.5: A computer generated image of the full calorimeter.

The ATLAS Calorimeter system, shown in Figure 2.5, is comprised of two main subsystems; the electromagnetic calorimeter (ECAL) and hadronic calorimeter (HCAL), which are designed to stop and measure the energy of electromagnetic-interacting and hadronic particles respectively. The combination of the two provides full coverage in ϕ and $|\eta| < 4.95$. Particles slow down and lose energy generating showers when crossing different layers. The ECAL is comprised of one barrel and two end-cap sectors employing liquid Argon (LAr). The showers hereby develop as electrons pairs which are then collected. The HCAL is also comprised of one barrel and two end-cap sectors. The sensors in the barrel of the HCAL are tiles of scintillating plastic whereas LAr is employed for the end-cap. A forward region, the closest possible to the beam, is covered by a LAr forward calorimeter (FCal). The LAr and Tile Calorimeter will be briefly discussed in the

605 following paragraphs.

606 The Liquid Argon Calorimeters

607 The ECAL is comprised of multiple layers of liquid Argon (LAr) sampler and lead ab-
 608 sorber. The choice of its accordion-geometry design brought two main advantages; full
 609 ϕ coverage with no non-interactive regions (no cracks); fast extraction of signals coming
 610 from both front or rear end of the electrodes. It is made of two half-barrel wheels, both
 611 placed in the barrel cryostat, that provide a pseudorapidity coverage up to $|\eta| < 1.475$
 612 and two end-cap detectors providing $1.375 \leq |\eta| \leq 3.20$ coverage in two end-cap cryo-
 613 stats. The junction between the barrel and end cap components defines the crack region
 614 and any signal coming from the crack region is therefore discarded.

615 In the $|\eta| < 1.8$ region there is an additional layer, placed at the front of the calorimeter,
 616 that is made of a thin (0.5 cm in the end-cap and 1.1 cm in the barrel) LAr layer with
 617 no absorber [28]. This additional layer was designed to correct for the energy lost, as
 618 particles enter the calorimeter, by taking a measurement just before the majority of the
 619 electromagnetic shower is developed.

620 The Tile calorimeter

621 The main purpose of the hadronic calorimeter is to measure the energy of hadronic showers.
 622 It is built employing steel and scintillating tiles coupled to optical fibres which are read
 623 out by photo-multipliers. As shown in Figure 2.5, the HCAL is made up of three cylin-
 624 ders; a central barrel, 5.64 m long covering a region $|\eta| < 1.0$, and two extended barrel,
 625 2.91 m long covering a reigon $0.8 < |\eta| < 1.7$. Each cylinder is made up of 64 modules
 626 and each module is in turn made up of three layers. Ultimately, the smallest section of the
 627 calorimeter module is a cell with a $\Delta\phi \times \Delta\eta = 0.1 \times 0.1$ granularity for the two innermost
 628 layers and $\Delta\phi \times \Delta\eta = 0.2 \times 0.1$ for the outermost one.

629 2.2.4 The Muon Spectrometer

630 The MS [29], shown in Figure 2.6, is the outermost sub-system of the whole ATLAS de-
 631 tector. As such, it surrounds the calorimeters and its main function is to perform precision
 632 measurement of muons momenta. The deflection of muon tracks employing large super-
 633 conducting air-core toroid magnets and high-precision tracking chambers is at the heart
 634 of such high precision measurement.

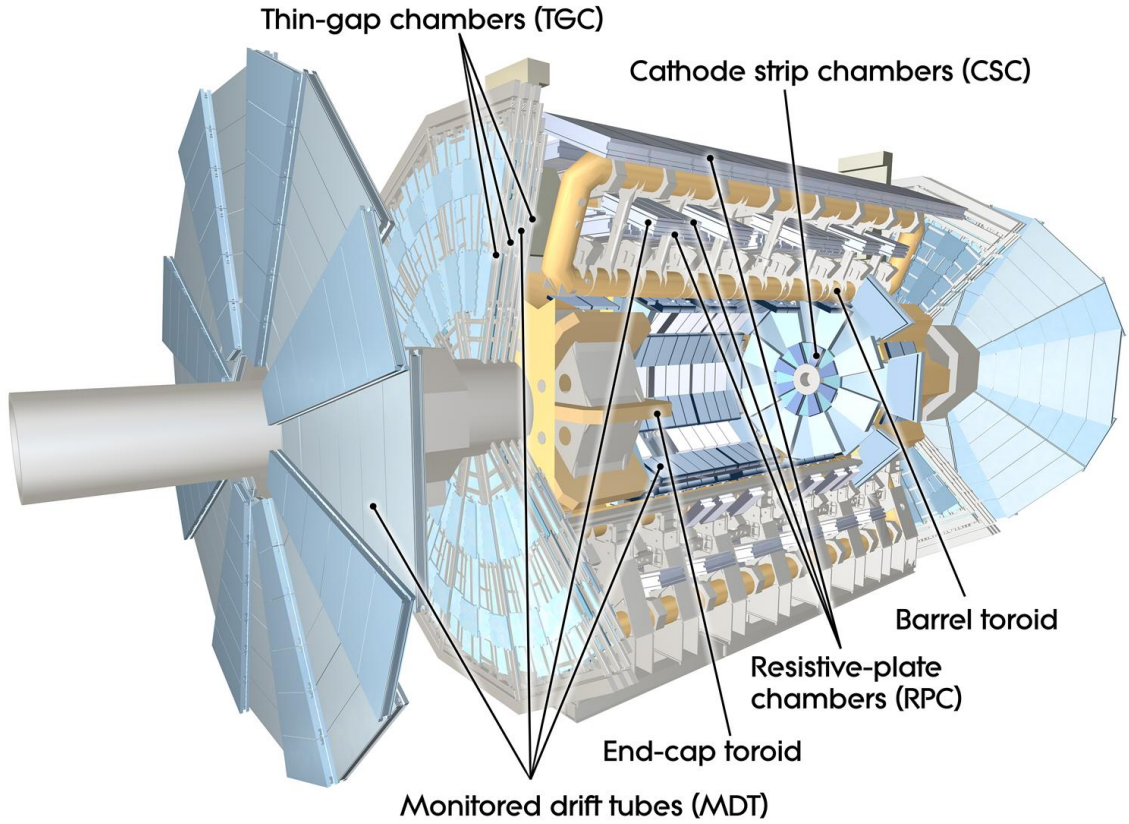


Figure 2.6: Cut-away view of the ATLAS muon system [4].

635 The MS is comprised of one large barrel toroid, covering the region $|\eta| \leq 1.4$, and
 636 two end-cap toroids, covering $1.6 < |\eta| \leq 2.7$ which are employed together to achieve the
 637 track-bending effect wanted. The magnitude of the magnetic field in the barrel, generated
 638 by eight large superconducting coils, ranges from 0.5 to 2 T.

639 Around the beam axis, three cylindrical layers make way for the chambers, placed in
 640 planes perpendicular to the beam, used to measure tracks.

641 Monitored Drift Chambers (MDTs) are employed over most of the pseudorapidity
 642 range to provide precision measurement of track coordinates in the bending direction.
 643 Cathode Strip Chambers (CSCs) are instead employed at large pseudorapidity ($2 < |\eta| <$
 644 2.7). Finally, in the end-cap regions Thin-Gap Chambers (TGCs) together with Resistive-
 645 Plate Chambers (RPCs) are dedicated to the Trigger System discussed in Section 2.3.

646 2.3 The ATLAS Trigger System

647 The ATLAS Trigger System is at the heart of data taking. It is an essential component of
 648 any nuclear or particle physics experiment since it is responsible for deciding whether or
 649 not to store an event for later study [5]. The ATLAS Trigger system is employed to reduce

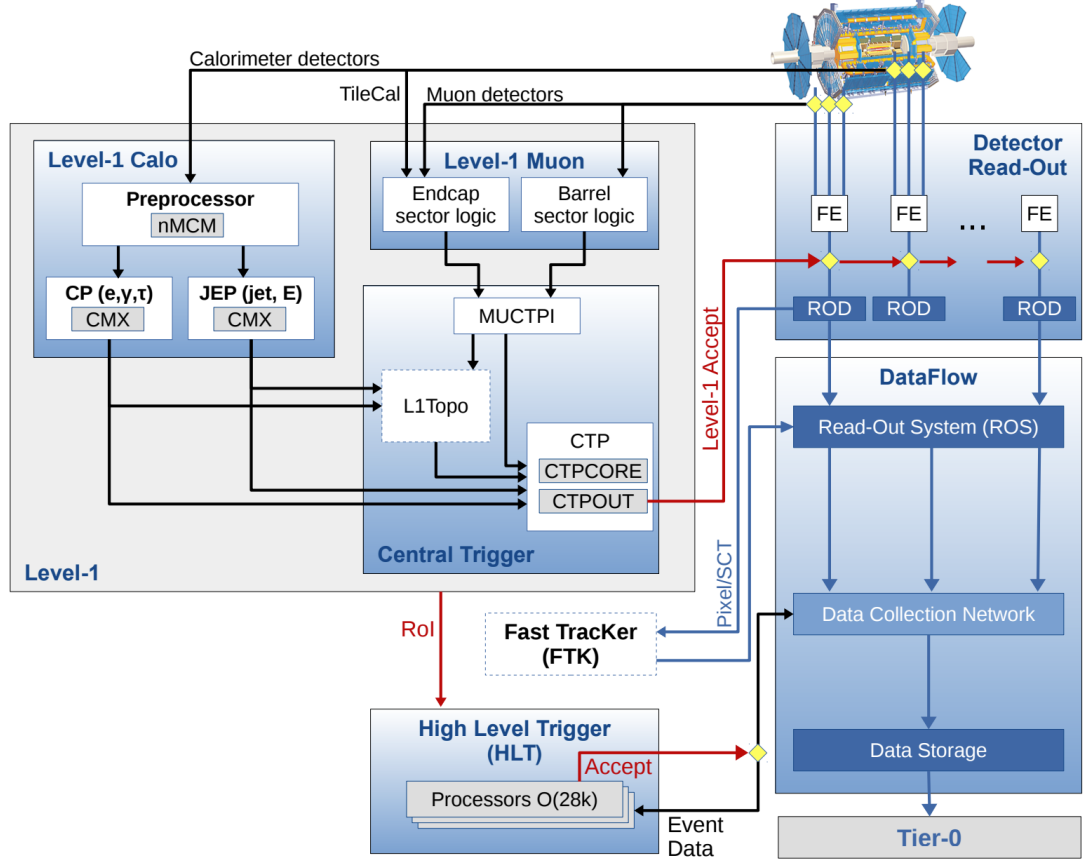


Figure 2.7: The ATLAS TDAQ system. L1Topo and FTK were being commissioned during 2015 and not used for the results shown in this thesis [5].

650 the event rate from $\sim 40 \text{ MHz}$ ¹ bunch-crossing² to $\sim 200 \text{ Hz}$ which corresponds to roughly
 651 300 MB/s.

652 The Trigger and Data Acquisition (TDAQ) system shown in Figure 2.7 consists of a
 653 hardware-based first level trigger (L1) and a software-based high-level trigger (HLT). The
 654 L1 trigger decision is formed by the Central Trigger Processor (CTP), which receives in-
 655 puts from the L1 calorimeter (L1Calo) and L1 muon (L1Muon) triggers. The first level
 656 (L1), which was designed to perform the first selection step, is a hardware-based system
 657 that uses information from the calorimeter and muon subdetectors. It also defines the
 658 so-called Regions of Interest (RoIs) within the detector to be investigated by the next level
 659 trigger, the HLT. Additionally, a Fast TracKer (FTK) system [30] (not yet installed) will
 660 provide global ID track reconstruction at the L1 trigger rate using lookup tables stored in

¹The LHC delivers beams with a bunch-spacing of 25 ns.

²The term bunch-crossing is hereby used when referring to a collision between two bunches of protons. Since only a certain fraction of the total momentum carried by each proton contributes to the collision, an average number of interactions per bunch-crossing, $\langle \mu \rangle$ is used.

661 custom associative memory chips for the pattern recognition. The FPGA-based track fitter
 662 will perform a fast linear fit and the tracks are made available to the HLT. This system will
 663 allow the use of tracks at much higher event rates in the HLT than is currently affordable
 664 using CPU systems. However, the upgrade of the ATLAS trigger will not be discussed
 665 any further.

666 In the next sections the L1 and HLT will be briefly described.

667 2.3.1 Level 1 Trigger

668 The Level 1 Trigger identifies Regions of Interest (RoIs)³ and passes these to HLT which
 669 will perform further investigations. Furthermore, in order to decide whether or not the
 670 event processing will continue, L1 selection uses only information coming from some
 671 parts of the detector to keep the input rate to a maximum of 100 kHz. L1 is implemented
 672 in fast custom electronics to keep the latency⁴ below 2.5 μ s. Event data from other sub-
 673 system are temporarily stored in memories whilst L1 decision is taken.

674 The L1 topological trigger (L1-Topo) [31] is feeded with energy and direction inform-
 675 ation, about the objects found by the L1 calorimeter and the muon trigger, which will be
 676 processed by dedicated algorithms implemented in its own FPGAs. However, due to the
 677 100 kHz read-out rate, not all the information collected by L1-Topo will be sent to the HLT,
 678 but only part of it. In order to properly seed the ROI-guided HLT reconstruction, specific
 679 objects in combination with the correct topological criteria must be employed.

680 2.3.2 High-Level Trigger

681 The HLT is used to reduce the output rate down to 1 kHz and it has a \sim 200 ms average
 682 decision time. Events that pass L1 trigger are then processed by the HLT using finer-
 683 granularity calorimeter information, precision measurements from the MS and tracking
 684 information from the ID. The HLT reconstruction can be run within RoIs identified at L1
 685 or a so-called full-scan on the full detector can be performed. The track reconstruction in
 686 the Inner Detector is an essential component of the trigger decision in the HLT and it will
 687 be discussed more in detail in Chapter 3

³ $\eta - \phi$ regions where event features have been found by the L1 selection process.

⁴Time needed by an electric signal to get to the front-end electronics.

688 **3** | The *b*-jet Trigger Signature in AT-
689 LAS

690 In this chapter the monitor and performance of the bottom-quark-initiated jet (*b*-jet) sig-
691 nature trigger, this being the author’s “technical/qualification task” to become a qualified
692 member of the experiment, will be discussed. The efficiencies of some of the Run 2 *b*-jet
693 triggers were evaluated using 3.8 fb^{-1} of pp collisions data collected in 2015 with 25 ns
694 bunch-spacing.

695 The qualification task

696 **3.1 Trigger Efficiency**

697 4 | Event Simulation and Reconstruction

698

699 bla bla bla

700 **4.1 Event Generation**

701 bla bla

702 **4.1.1 Parton Distribution Functions (PDFs)**

703 bla bla bla

704 **4.1.2 Matrix Element Calculation**

705 bla bla bla

706 **4.1.3 Parton Showers**

707 bla bla bla

708 **4.1.4 Hadronisation**

709 bla bla bla

710 **4.2 Detector Simulation**

711 bla bla bla

⁷¹² **5**⁷¹³⁷¹⁴

Stop searches in final states with jets and missing transverse energy

⁷¹⁵ **6** | Results and Statistical Interpretations

⁷¹⁶

⁷¹⁷ Trigger

⁷¹⁸ bla vlas bla

Bibliography

- [1] ATLAS Collaboration, “Summary plots from the atlas standard model physics group.”
https://atlas.web.cern.ch/Atlas/GROUPS/PHYSICS/CombinedSummaryPlots/SM/ATLAS_a_SMSummary_TotalXsect/ATLAS_a_SMSummary_TotalXsect.png. viii, 9
- [2] C. Borschensky, M. Krämer, A. Kulesza, M. Mangano, S. Padhi, T. Plehn, and X. Portell, *Squark and gluino production cross sections in pp collisions at $\sqrt{s} = 13, 14, 33$ and 100 TeV*, *Eur. Phys. J.* **C74** no. 12, (2014) 3174, [arXiv:1407.5066 \[hep-ph\]](https://arxiv.org/abs/1407.5066). viii, 16
- [3] C. Lefèvre, *The CERN accelerator complex*, <http://cds.cern.ch/record/1260465>. viii, 20, 21
- [4] ATLAS Collaboration, *The ATLAS experiment at the CERN Large Hadron Collider*, *Journal of Instrumentation* **3** no. 08, (2008) S08003.
<http://stacks.iop.org/1748-0221/3/i=08/a=S08003>. ix, 22, 28
- [5] A. Collaboration, *Performance of the ATLAS Trigger System in 2015*, *Eur. Phys. J.* **C77** (2017), [arXiv:1611.09661 \[hep-ex\]](https://arxiv.org/abs/1611.09661). ix, 28, 29
- [6] M. Herrero, *The Standard Model*, <https://arxiv.org/abs/hep-ph/9812242>. 2
- [7] ATLAS Collaboration, *Observation of a New Particle in the Search for the Standard Model Higgs Boson with the ATLAS Detector at the LHC*, *Phys.Lett.* **B716** (2012), [arXiv:1207.7214 \[hep-ex\]](https://arxiv.org/abs/1207.7214). 2
- [8] CMS Collaboration, *Observation of a new boson at a mass of 125 GeV with the CMS experiment at the LHC*, *Phys.Lett.* **B716** (2012), [arXiv:1207.7235 \[hep-ex\]](https://arxiv.org/abs/1207.7235). 2
- [9] A. Pich, *The Standard Model of Electroweak Interactions*, [arXiv:1201.0537 \[hep-ph\]](https://arxiv.org/abs/1201.0537). 5, 6

- ⁷⁴³ [10] K. A. Olive at al. (Particle Data Group), *Review of Particle Physics*, **Chin.Phys. C** **38**(9) (2014). 6
- ⁷⁴⁵ [11] J. Goldstone, A. Salam and S. Weinberg, *Broken Symmetries*, **Phys. Rev.** **127** (1962) 965–970. 8
- ⁷⁴⁷ [12] S. Weinberg, *Implications of Dynamical Symmetry Breaking*, **Phys. Rev.** **D19** (1976) 1277–1280. 10
- ⁷⁴⁹ [13] Super-Kamiokande Collaboration, Y. Fukuda et al., *Evidence for oscillation of atmospheric neutrinos*, **Phys. Rev. Lett.** **81** (1998) 1562–1567, [arXiv:hep-ex/9807003 \[hep-ex\]](https://arxiv.org/abs/hep-ex/9807003). 10
- ⁷⁵² [14] SNO Collaboration, *Measurement of the Rate of $\nu_e + d \rightarrow p + p + e^-$ Interactions Produced by 8B Solar Neutrinos at the Sudbury Neutrino Observatory*, **Phys. Rev. Lett.** **87** (2001). 10
- ⁷⁵⁵ [15] T. O. W. of the Nobel Prize.
⁷⁵⁶ https://www.nobelprize.org/nobel_prizes/physics/laureates/2015/. 10
- ⁷⁵⁷ [16] F. Jegerlehner, *The hierarchy problem of the electroweak Standard Model revisited*, [arXiv:1305.6652 \[hep-ph\]](https://arxiv.org/abs/1305.6652). 12
- ⁷⁵⁹ [17] Johan Alwall, Philip C. Schuster and Natalia Toro, *Simplified models for a first characterization of new physics at the LHC*, **Phys. Rev. D** **D79** (2009). 16
- ⁷⁶¹ [18] J.M. Jowett, M. Schaumann, R. Alemany, R. Bruce, M. Giovannozzi, P. Hermes, W. Hofle, M. Lamont, T. Mertens, S. Redaelli, J. Uythoven, J. Wenninger, *The 2015 Heavy-Ion Run of the LHC*, <http://accelconf.web.cern.ch/accelconf/ipac2016/papers/tupmw027.pdf>. 19
- ⁷⁶⁵ [19] O. S. Brüuning, P. Collier, P. Lebrun, S. Myers, R. Ostojic, J. Poole and P. Proudlock, *LHC Design Report*, <https://cds.cern.ch/record/782076>. 20
- ⁷⁶⁷ [20] CMS Collaboration, *The CMS experiment at the CERN LHC*, **Journal of Instrumentation** **3** no. 08, (2008) S08004.
⁷⁶⁹ <http://stacks.iop.org/1748-0221/3/i=08/a=S08004>. 20
- ⁷⁷⁰ [21] LHCb Collaboration, et. al, *The LHCb Detector at the LHC*, **JINST** (2008). 20

- 771 [22] ALICE Collaboration, *The ALICE experiment at the CERN LHC*, Journal of
 772 Instrumentation **3** no. 08, (2008) S08002.
 773 <http://stacks.iop.org/1748-0221/3/i=08/a=S08002>. 20
- 774 [23] A. Yamamoto, Y. Makida, R. Ruber, Y. Doi, T. Haruyama, F. Haug, H. ten Kate,
 775 M. Kawai, T. Kondo, Y. Kondo, J. Metselaar, S. Mizumaki, G. Olesen, O. Pavlov,
 776 S. Ravat, E. Sbrissa, K. Tanaka, T. Taylor, and H. Yamaoka, *The ATLAS central*
 777 *solenoid*, Nuclear Instruments and Methods in Physics Research Section A:
 778 Accelerators, Spectrometers, Detectors and Associated Equipment **584** no. 1, (2008)
 779 53 – 74.
 780 <http://www.sciencedirect.com/science/article/pii/S0168900207020414>. 22,
 781 23
- 782 [24] ATLAS Collaboration, *The ATLAS Inner Detector commissioning and calibration*, Eur.
 783 Phys. JC**70** , [arXiv:1004.5293](https://arxiv.org/abs/1004.5293). 23
- 784 [25] ATLAS Collaboration, *ATLAS Insertable B-Layer Technical Design Report*,
 785 <https://cds.cern.ch/record/1291633>. 24
- 786 [26] G. A. et al., *ATLAS pixel detector electronics and sensors*, Journal of Instrumentation **3**
 787 no. 07, (2008) P07007. <http://stacks.iop.org/1748-0221/3/i=07/a=P07007>. 25
- 788 [27] A. Bingül, *The ATLAS TRT and its Performance at LHC*, Journal of Physics:
 789 Conference Series **347** no. 1, (2012) 012025.
 790 <http://iopscience.iop.org/article/10.1088/1742-6596/347/1/012025/meta>.
 791 25
- 792 [28] ATLAS Collaboration, *ATLAS liquid-argon calorimeter: Technical Design Report*,
 793 <https://cds.cern.ch/record/331061>. 27
- 794 [29] ATLAS Collaboration, *ATLAS muon spectrometer: Technical design report*,
 795 <https://cds.cern.ch/record/331068>. 27
- 796 [30] ATLAS Collaboration, *Fast TracKer (FTK) Technical Design Report*,
 797 <https://cds.cern.ch/record/1552953>. 29
- 798 [31] E. Simoni, *The Topological Processor for the future ATLAS Level-1 Trigger: from design to*
 799 *commissioning*, [arXiv:1406.4316](https://arxiv.org/abs/1406.4316). 30